

PAPER

# Properties of a new quasi-axisymmetric configuration

To cite this article: S.A. Henneberg *et al* 2019 *Nucl. Fusion* **59** 026014

View the [article online](#) for updates and enhancements.

# Properties of a new quasi-axisymmetric configuration

S.A. Henneberg<sup>1</sup> , M. Drevlak<sup>1</sup>, C. Nührenberg<sup>1</sup>, C.D. Beidler<sup>1</sup> , Y. Turkin<sup>1</sup>, J. Loizu<sup>2</sup> and P. Helander<sup>1</sup> 

<sup>1</sup> Max-Planck-Institut für Plasmaphysik, Wendelsteinstr. 1, 17489 Greifswald, Germany

<sup>2</sup> École Polytechnique Fédérale de Lausanne (EPFL), Swiss Plasma Center (SPC), CH-1015 Lausanne, Switzerland

E-mail: [Sophia.Henneberg@ipp.mpg.de](mailto:Sophia.Henneberg@ipp.mpg.de)

Received 6 September 2018, revised 15 November 2018

Accepted for publication 4 December 2018

Published 4 January 2019



## Abstract

A novel, compact, quasi-axisymmetric configuration is presented which exhibits low fast-particle losses and is stable to ideal magnetohydrodynamic (MHD) instabilities. The design has fast-particle loss rates below 8% for flux surfaces within the half-radius, and is shown to have a MHD stability limit of a normalized pressure of  $\langle\beta\rangle = 3\%$ , where  $\langle\beta\rangle$  is volume averaged. The flux surfaces at various plasma betas and currents as calculated using the SPEC equilibrium code (Loizu *et al* 2016 *Phys. Plasmas* **23** 112505) are presented. Neoclassical transport coefficients are shown to be similar to an equivalent tokamak, with a distinct banana regime at half-radius. An initial coil design study is presented to assess the feasibility of this configuration as a fusion-relevant experiment.

Keywords: stellarator optimization, quasi-axisymmetry, stellarator design study

(Some figures may appear in colour only in the online journal)

## 1. Introduction

Similarly to tokamaks, quasi-axisymmetric (QA) equilibria possess a magnetic field strength that is symmetric in the toroidal Boozer coordinate; they thus share many neoclassical properties with tokamaks. These configurations are capable of being compact thanks to their relatively large bootstrap current which provides a source of rotational transform, in addition to that from the coils. On the other hand, the similarity to stellarators provides potential benefits: QA configurations can run in steady state potentially without any current drive, and there is evidence from other types of stellarators that disruptions can be avoided if the vacuum rotational transform, created solely by the coils, is sufficiently large [2–4]. The related concept of quasi-helical symmetry was numerically proven in 1988 [5] and experimentally confirmed in a series of experiments on the HSX stellarator [6, 7].

Good confinement in quasi-symmetric fields is ensured by the existence of a third constant of the guiding-centre motion besides the energy and the magnetic moment to confine the guiding-centre orbits [8]. The guiding-centre Lagrangian in

Boozer coordinates  $(\psi, \theta, \phi)$  [9] only depends on the magnetic field strength rather than the direction of the magnetic field:

$$L = \frac{m}{2B^2} (I\dot{\theta} + G\dot{\phi})^2 + Ze(\psi\dot{\theta} - \chi\dot{\phi}) - \mu B - Ze\Phi \quad (1)$$

where  $m$  is the mass,  $B$  is the magnetic field strength,  $I$  and  $G$  are the toroidal and poloidal current, respectively,  $Ze$  is the charge,  $\chi$  is the poloidal flux,  $\mu$  is the magnetic moment and  $\Phi$  is the electrostatic potential [10].

One obtains a third invariant (in addition to  $\mu$  and the energy) if the magnetic field strength  $B$  and the scalar potential  $\Phi$  only depend on two of the magnetic coordinates (e.g.  $\theta$  and  $\psi$ ). The canonical momentum corresponding to the third magnetic coordinate ( $\phi$ ) is then conserved:

$$\dot{p}_\phi = \frac{\partial L}{\partial \phi} = 0. \quad (2)$$

The first QA equilibria were presented in 1994 [11] and 1996 [12]. They were followed by many more designs such as NCSX [13], CHS-qa [14] and ESTELL [15], none of which have been constructed. The aim of the present design is slightly different. Here we aim for a compact (aspect ratio of 3 to 4),

magnetohydrodynamic (MHD)-stable configuration with small fast-particle loss rates, so that the device could, at least in principle, scale up to a reactor. A compact, MHD-stable equilibrium has been designed before (e.g. NCSX, CHS-qa), but we simultaneously require improved fast-particle loss rates compared with previous designs.

The paper is organized as follows. In section 2 we describe the methods used to obtain the new configuration, including a description of the optimization code ROSE and the criteria which were targeted. The main section of this paper (section 3) provides an overview of the new configuration including the geometrical properties of the new equilibrium design (section 3.1), results of fast-particle loss-fraction calculations (section 3.2), stability calculations (section 3.3), preliminary results of islands and chaotic region development with varying plasma beta and current (section 3.4), neoclassical transport and bootstrap calculations (section 3.5) and a preliminary coil set (section 3.6). The paper finishes with a summary and ideas for future work.

## 2. Optimization methods

The optimization tool ROSE (ROSE optimizes stellarator equilibria [16]) was exploited to examine the configuration space of ideal-MHD plasma boundaries. The standard optimization method is Brent's algorithm, which combines several root-finding methods such as the secant method, bisection method and a quadratic-inverse algorithm [17]. The cost function  $f$  which is optimized is evaluated with the weighted sum method:

$$f = \sum_i w_i (F_i - \tilde{F}_i)^2, \quad (3)$$

where  $w_i$  are weights which have to be adapted for obtaining various configurations on the Pareto frontier<sup>3</sup>. The latter is the set of optima where an optimum configuration is defined such that one cannot improve any criterion without worsening at least one other criterion. In equation (3),  $F_i$  is the value for the criterion,  $i$ , and  $\tilde{F}_i$  is the corresponding target value. ROSE uses several other codes, including VMEC [18], a modified NESCOIL [19] and VM2MAG [20], and is capable of analysing many different criteria, including physical, geometrical and coil design properties.

For the plasma boundary optimization, we used the fixed-boundary equilibrium mode of VMEC. In this mode, VMEC represents the plasma boundary with a set of two Fourier series:

$$\begin{aligned} r(u, v) &= \sum r_{m,n} \cos(2\pi(mu - nNv)), \quad z(u, v) \\ &= \sum z_{m,n} \sin(2\pi(mu - nNv)), \end{aligned} \quad (4)$$

where  $r$  and  $z$  are cylindrical coordinates,  $u$  is the VMEC poloidal angle and  $v$  is the VMEC toroidal angle.

For the configuration presented here, the chosen input parameters are:

<sup>3</sup> If the Pareto frontier is non-convex, there are points on it that cannot be found by this method.

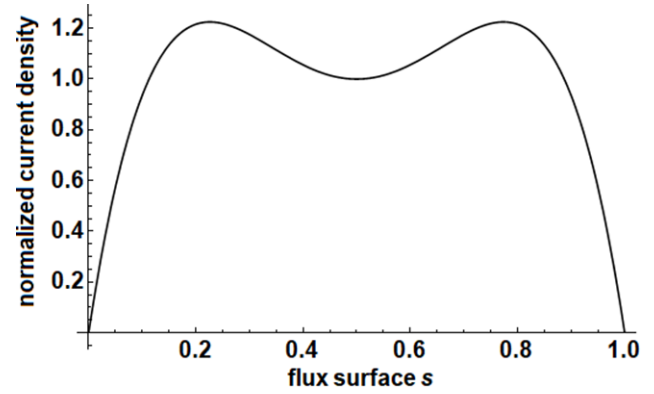


**Figure 1.** Normalized current density profile versus normalized flux  $s$  for a bootstrap-like scenario. This profile is normalized to the total toroidal current; at the reactor size, the total toroidal current is approximately 2.5 MA.

- aspect ratio  $A = \frac{R}{a}$ , where  $R = r_{0,0}$  and  $a = \sqrt{r_{1,0}^2 + z_{1,0}^2}$  are the approximate major and minor radii of the plasma, respectively,
- number of field periods,
- volume-averaged plasma beta,  $\beta = \frac{2\mu_0 p}{B^2}$ , where  $p$  is the plasma pressure and  $\mu_0$  is the vacuum permeability.

The targeted parameters for the optimization are:

- rotational transform,  $\iota$ , at the magnetic axis and at the plasma boundary,
- vacuum rotational transform at the magnetic axis,
- vacuum magnetic well  $\frac{\partial}{\partial \psi} \int_{-\infty}^{\infty} \frac{dl}{B} < 0$ , where the integration is along a magnetic field line,
- the integrated absolute value of the Gaussian curvature of the plasma boundary,
- the quasi-axisymmetric error  $\frac{\sqrt{\sum_{n \neq 0, m} B_{m,n}^2}}{B_{00}}$  where the magnetic field strength is given by  $B = \sum_{m,n} B_{m,n} \cos(m\theta + nN\phi)$ .

We anticipate that the bootstrap current is sufficient to be the only net current in the plasma (e.g. no ohmic current is required). This is supported by preliminary calculations with the one-dimensional (1D) transport code NTSS [21]. We therefore used a bootstrap-like current density profile for optimization (see figure 1).

We aimed for a vacuum rotational transform above 0.3 and forced the total rotational transform to stay below 0.5 everywhere in the plasma by targeting the boundary rotational transform to stay below this value (see figure 2(a)) in order to avoid the  $\iota = 1/2$  rational surface, in the interest of MHD stability.

It can be shown that quasi-axisymmetry can only be achieved exactly on one single flux surface [22, 23], and we therefore only minimized the QA error on one designated flux surface. Parameter scans are obtained by varying this flux surface between the magnetic axis and the plasma boundary (see figure 3). The best fast-particle confinement is achieved where the QA error is minimized at the flux surfaces  $s_{\text{qa}} = 0.4$  and  $s_{\text{qa}} = 0.5$ . The normalized toroidal flux surface  $s$  is defined as  $s = \frac{\psi}{\psi_a}$  with  $\psi_a$  the magnetic flux at the plasma boundary.

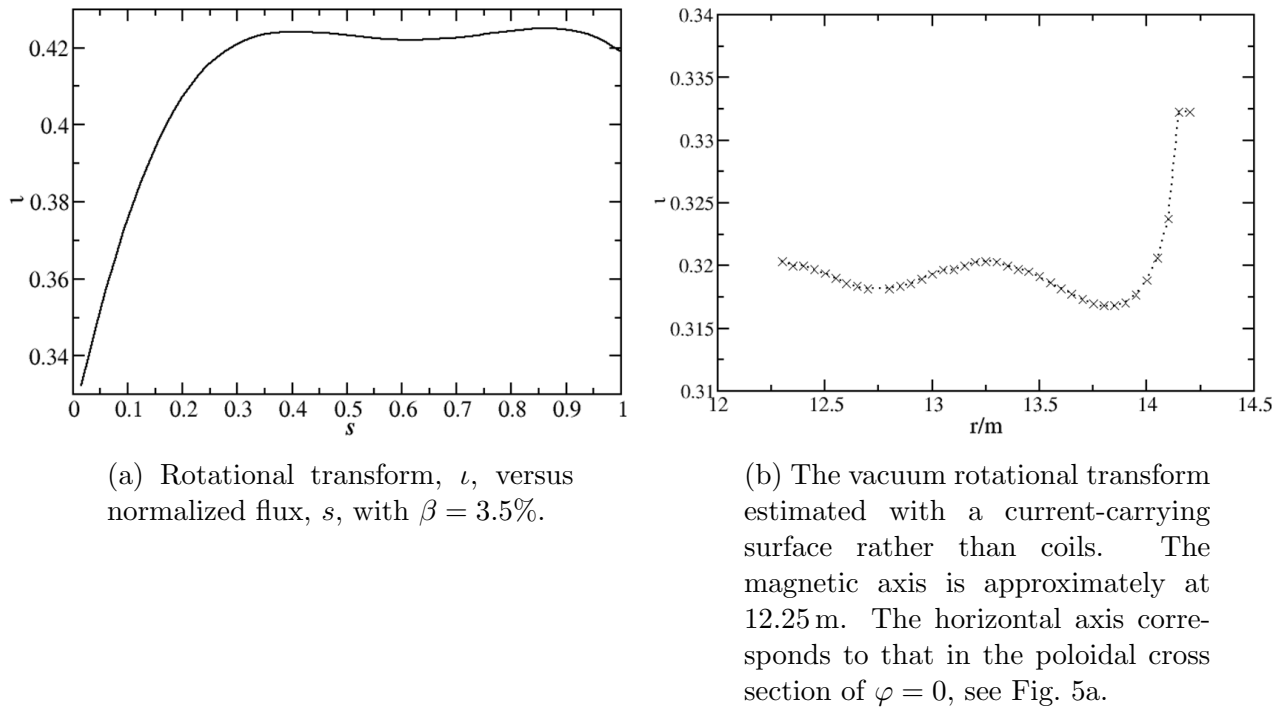


**Figure 2.** Rotational transform profiles for the new configuration at  $\beta = 3.5\%$  and  $\beta = 0\%$ .

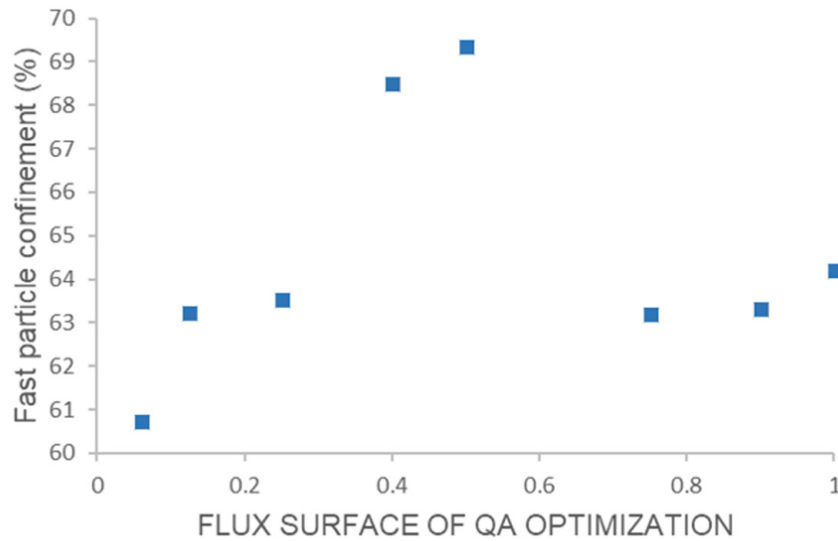


**Figure 3.** The effect of varying the location for the QA error optimization: the cumulative percentage of particles which remain inside the plasma for each optimized configuration versus the location of QA optimization.

Of those two configurations we chose the configuration with a higher vacuum magnetic well for stability reasons (with  $s_{qa} = 0.4$ ). We will report on these scans in greater depth in a future paper. The following section describes the final configuration, as illustrated in figure 4.

### 3. The new design—an overview

#### 3.1. Configuration specification

The configuration was optimized with an aspect ratio of 3.4, two field periods, a volume-averaged plasma beta of 3.5% and a pressure profile  $\sim 1 - 0.8s + 1.3s^2 - 1.5s^3$  (see

figure 4(a)). A primary design objective was compactness, which is an advantage of the QA configuration, and therefore an aspect ratio below 4 was considered to be desirable. The choice of two field periods facilitates the design of a modular coil set for low aspect ratios. The rotational transform profile of the optimized design lies between 0.3 and 0.5 (see figure 2(a)) so that the low-order rational  $\frac{1}{2}$  is avoided. The scaled plasma current has a total value of 2.5 MA at reactor size ( $V = 1900 \text{ m}^3$ ). The flat vacuum-rotational-transform profile is shown in figure 2(b). It varies between 0.317 and 0.332, and therefore  $8/25 = 0.32$  is the rational mode number with the smallest denominator in the

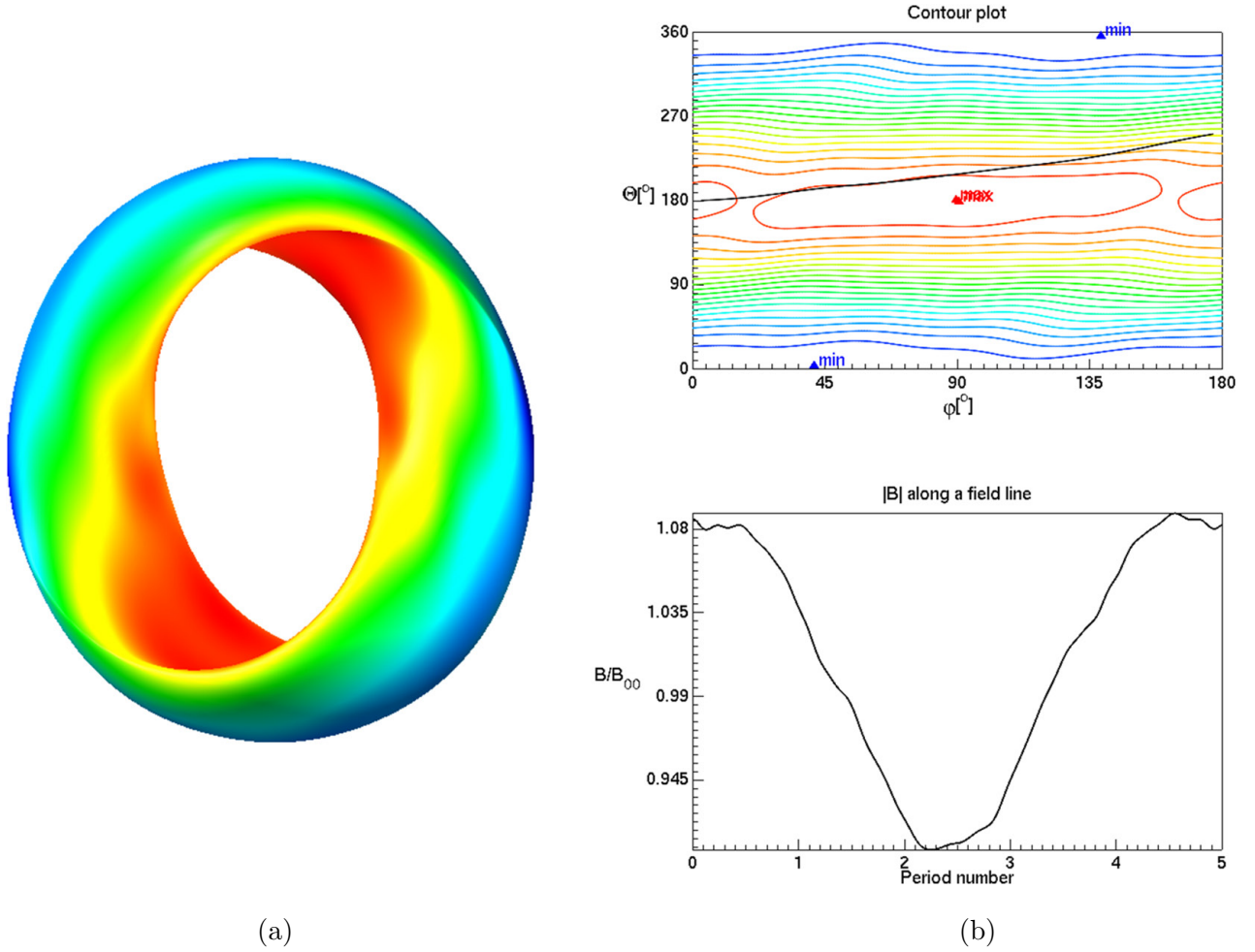


**Figure 4.** Magnetic field strength structure at the plasma boundary and at half-radius. (a) The magnetic field strength on the plasma boundary of the new equilibrium design. (b) Top: the contours of the magnetic field strength at half-radius ( $s = 0.25$ ) and a field line starting at  $\phi = 0^\circ$  and  $\theta = 180^\circ$ . Bottom: the magnetic field strength along a magnetic field line starting at  $\phi = 0^\circ$  and  $\theta = 180^\circ$ . Each period is equivalent to a step size of  $\Delta\phi = 180^\circ$ .

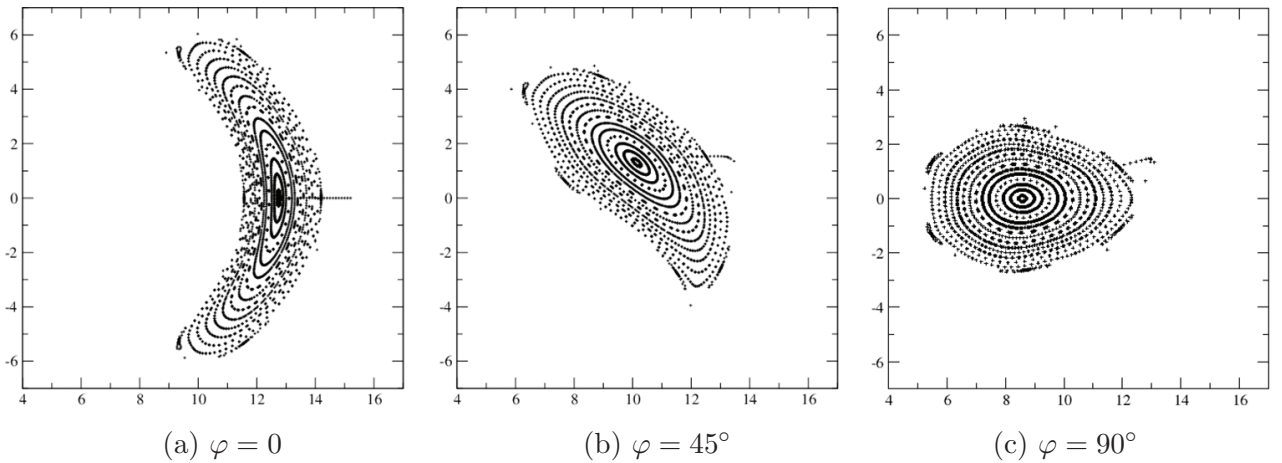


**Figure 5.** Poincaré plots of the cross sections of the estimated vacuum field. These plots indicate nested magnetic surfaces. In a vacuum, islands can potentially only appear at high-order rational flux surfaces since the vacuum rotational transform avoids low-order rationals besides the plasma boundary where the rotational transform is close to  $2/6$ .

vacuum-rotational-transform profile besides near the plasma boundary where it is close to  $2/6 \approx 0.333$ . The Poincaré plots of the vacuum magnetic field indicate nested magnetic surfaces (see figure 5). This is beneficial for the start-up of the device where there will be no plasma current to increase

the rotational transform profile to its targeted profile. All vacuum parameters were calculated assuming a continuous current-carrying winding surface using the virtual-casing principle [24]. They therefore depend on the realization of discrete coils, which are not yet finalized. For  $\beta = 3.5\%$ , the

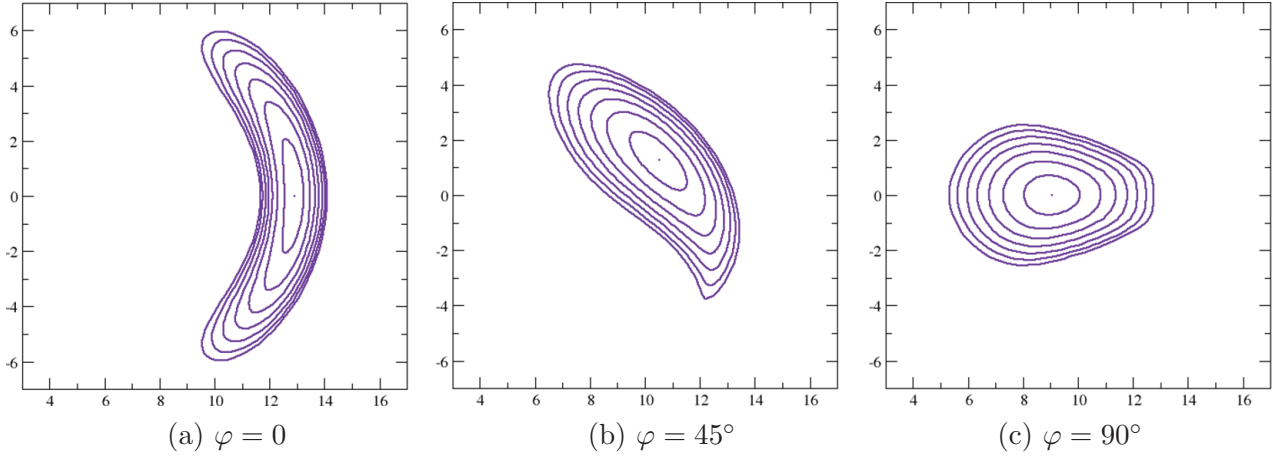


**Figure 6.** The flux surfaces at different toroidal angles  $\varphi$  and with  $\beta = 3.5\%$  as calculated by VMEC.

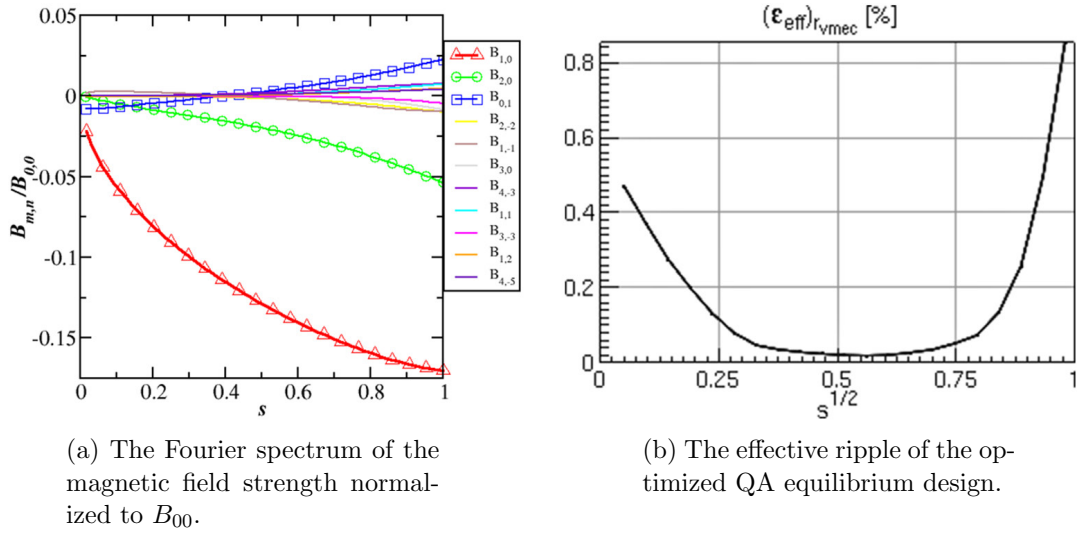
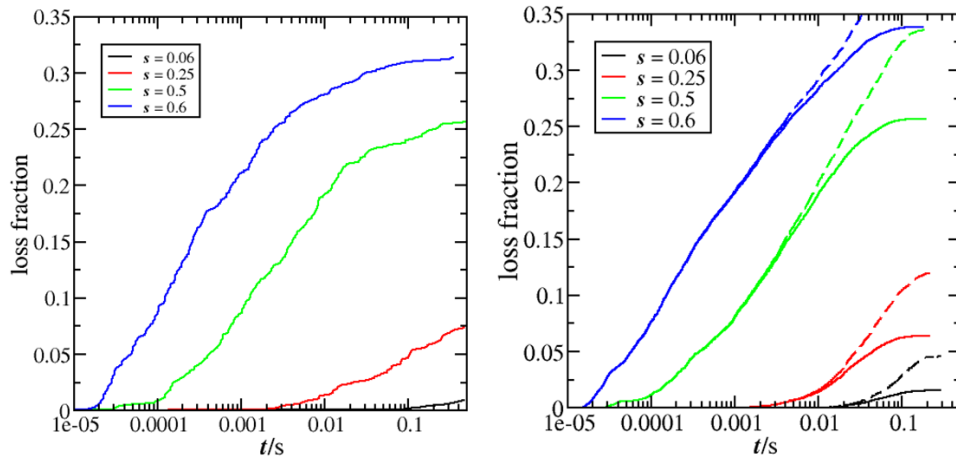


**Figure 7.** Magnetic field strength spectrum (left) and the effective ripple profile (right).



(a) The fast particle loss fraction at flux surfaces between  $s = 0.06$  and  $s = 0.6$  with the original parameters and with a plasma volume of  $1900\text{m}^3$ .

(b) The loss fraction of fast particles (dashed lines) and energy (solid lines) including collisions with the background plasma and accounting for an electric field.

**Figure 8.** Rates of fast-particle losses as calculated with ANTS.



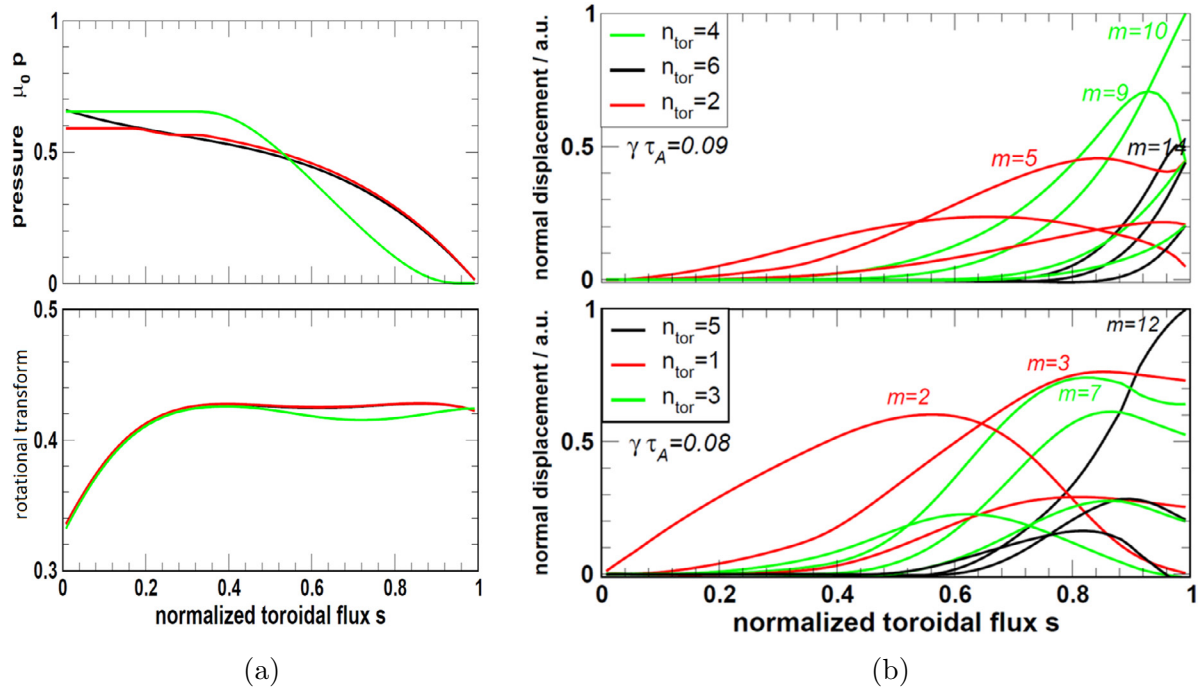


**Figure 9.** Pressure profiles with related rotational transform profiles and mode structures for  $\beta \approx 3.5\%$ . (a) Top: black, un-flattened pressure profile; green, red, altered profiles. Bottom: associated rotational transform profiles with fixed current density profiles. (b) Unstable modes. Top: mode structure for the red pressure profile (flattened only near the magnetic axis). Bottom: mode structure for green pressure profile (flattened near magnetic axis and near edge), this mode structure is less local than that for the other case.

poloidal cross sections of the flux surfaces calculated with VMEC at the toroidal angle  $\varphi = 0, 45^\circ, 90^\circ$  are displayed in figure 6. The magnetic field strength on the plasma boundary is shown in figure 4(a). Figure 4(b) illustrates the (quasi-) axisymmetric magnetic field structure at half-radius. The QA error is smallest around the flux surface  $s = 0.4$ , but increases towards the plasma edge and towards the plasma axis, as one would expect from theory [22]. As mentioned before, the QA error was optimized on various flux surfaces between  $s = 0.25$  and  $s = 0.5$ . This is also reflected in the Fourier spectrum of the magnetic field strength (see figure 7(a)) where the leading components of the magnetic field strength normalized to  $B_{00}$  are shown. All the non-QA components of the magnetic field strength are smaller than 2.5% of  $B_{00}$ . The leading non-QA component is the mirror term  $B_{01}$ , which has a maximum near the plasma edge. The other components are smaller than 1% throughout the entire plasma. The effective ripple  $\epsilon_{\text{eff}}$ , which is a measure of neoclassical transport [25], attains values between 0.01% at approximately half-radius and 0.6% at the edge, and lies below 0.2% in most of the plasma volume (see figure 7(b)). This is a side effect of the improved quasi-axisymmetry (since perfect quasi-symmetry implies  $\epsilon_{\text{eff}} = 0$ ) rather than the result of explicit optimization.

### 3.2. Fast-particle confinement

To determine whether this magnetic configuration could be relevant for a reactor, the alpha-particle (with energies of 3.5 MeV) confinement was investigated. The fast-particle loss fraction was evaluated with the drift orbit code ANTS (plasma simulation with drift and collisionS) [26]. The

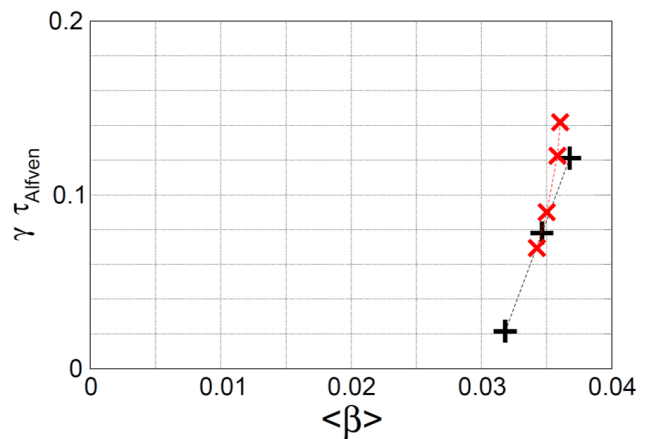


**Figure 10.** Ideal MHD stability  $\beta$ -limit: dependence of the growth rate on average plasma beta. The red points correspond to the pressure profile which has been flattened near the magnetic axis. The black points correspond to the pressure profile flattened at both the magnetic axis and the plasma boundary (see figure 9(a)). At  $\langle \beta \rangle$  below 3% ideal MHD stability prevails.

configuration was scaled to reactor size with a volume of 1900 m<sup>3</sup>, a major radius of 10.3 m, and a minor radius of 3.1 m, with a volume-averaged magnetic field of 5 T. Two results are presented here: one where the guiding centre drifts are calculated without any collisions (figure 8(a)) and the other including collisions with the background plasma and an electric field (figure 8(b)). In the case with collisions, specific density profiles of deuterium and tritium were imposed. Using these profiles, the temperature and radial electric field were self-consistently determined following a similar procedure to that which is described in [27]. One thousand

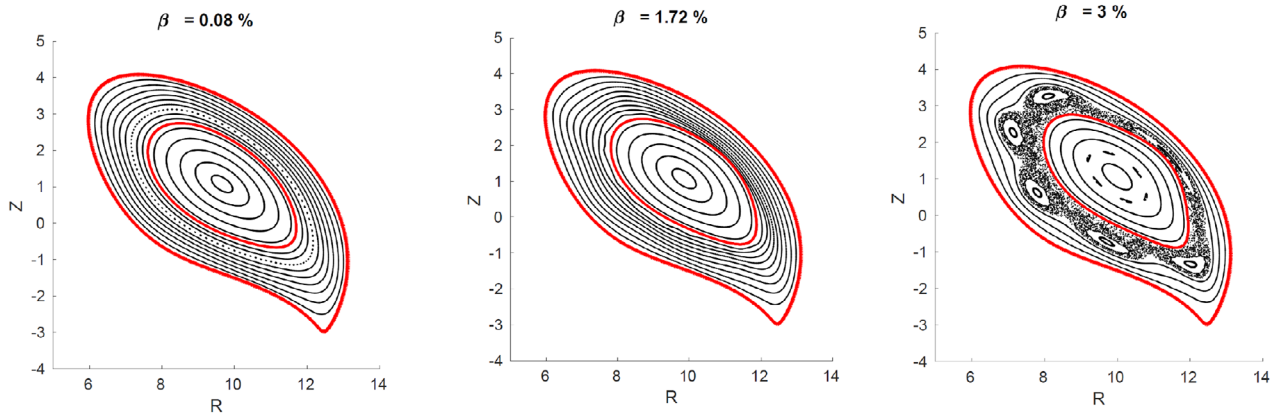


**Figure 11.** Poincaré plots of the poloidal cross section at  $\varphi = 37.5^\circ$  and with  $I_\phi = 0$  at (from left to right)  $\beta = 0.08\%$ ,  $1.72\%$  and  $3\%$  calculated by SPEC with the plasma boundary fixed. The inner red surface which is at  $s = 0.3$  indicates the position of the pressure step.

test particles, equally distributed on a flux surface, were launched with uniformly distributed pitch angles and traced for half a second. In the collisionless case the loss fraction is below 1% for the flux surface  $s = 0.06$  ( $r \approx 0.25$ ) and for the flux surface  $s = 0.25$  (approximately half-radius) it is 7.4% (see figure 8(a)). In the case including collisions with the background plasma, the particles are lost more quickly than without collisions (because of collisional scattering onto collisionless loss orbits); however, the energy losses are comparable to those without collisions (see figure 8(b)). Note that the curves describing particle and energy losses start to diverge after approximately one slowing-down time, which is about 0.03 s for  $s = 0.06$ .

### 3.3. Stability

As described above, one of the main advantages of QA configurations compared with tokamaks is their potential for being more stable and, hopefully, free from disruptions. The ideal MHD stability of the configuration was evaluated with the CAS3D code [28] in its free-boundary version. Three different pressure profiles were examined (see figure 9(a)). For the stability calculation, the equilibrium pressure profiles were chosen to be flat,  $p'(s) = 0$ , near the magnetic axis, where there are some low-order rational surfaces (e.g.  $\iota = 2/5$ ) in figure 2(a) for the finite- $\beta$  case. In this way, diverging parallel current densities are eliminated that appear in ideal MHD equilibria instead of magnetic islands [9, 10]. This flattening of the pressure profile only has a small effect on the rotational transform profile (see figure 9(a)). For  $\beta \approx 3.5\%$  the plasma is ballooning unstable. The Fourier harmonics of the displacement in the direction normal to the flux surfaces are shown in figure 9(b). The ballooning nature of the modes, as well as their free-boundary nature, is evident from the high amplitudes near the plasma boundary. By reducing the plasma beta and keeping the normalized profile fixed, a  $\beta$ -stability limit of 3% is determined for the chosen numerical parameters (see figure 10). This scan was performed with a fixed current profile and a fixed plasma boundary (figure 6).

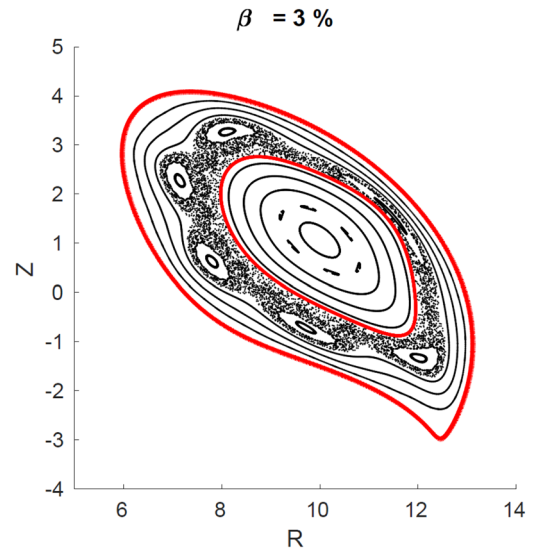


**Figure 12.** Enlarged Poincaré plot of the poloidal cross section at  $\varphi = 37.5^\circ$  with  $I_\phi = 0$  at  $\beta = 3\%$  calculated by SPEC with the plasma boundary fixed. A chain of six islands is visible.

### 3.4. Flux surfaces with varying $\beta$ and current

Magnetic surfaces are not guaranteed to exist in general three-dimensional MHD equilibria without continuous symmetry [29, 30]. While the vacuum field can be designed to possess nested magnetic surfaces (see figure 5), plasma currents are necessarily present at finite plasma pressure and thus the magnetic surfaces can potentially be destroyed at finite  $\beta$ . Moreover, the design presented herein considers a finite net toroidal current,  $I_\phi$ , and thus we must also assess whether this current can degrade (or improve) the quality of the confinement. Following the procedure described in [31], we use SPEC (the stepped-pressure equilibrium code) [1, 32] in order to assess the possible formation of magnetic islands and magnetic-field-line chaos at different values of  $\beta$  and  $I_\phi$ . A simplified pressure profile is assumed with  $p(s) = p_0$  for  $s \leq 0.3$  and  $p(s) = 0$  for  $s \geq 0.3$ . In this way, the pressure gradient and the pressure-driven (bootstrap) current density are concentrated on a single flux surface. In each of



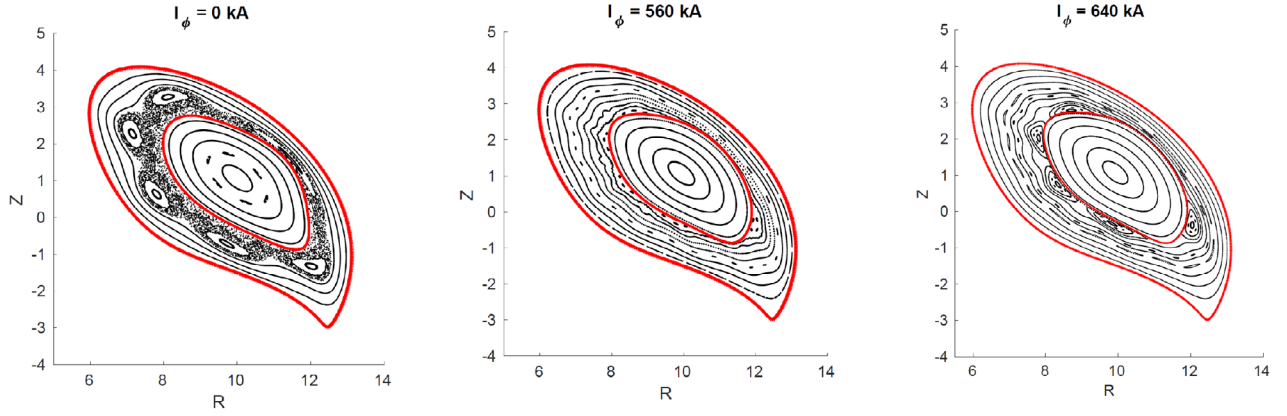
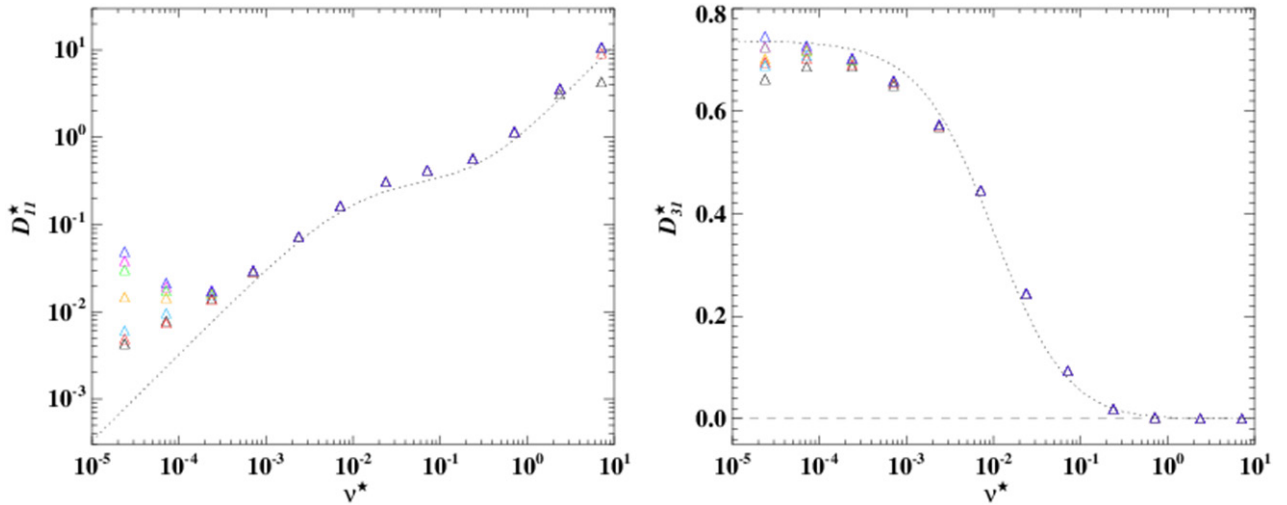


**Figure 13.** Poincaré plots of the poloidal cross section at  $\varphi = 37.5^\circ$  with constant  $\beta = 3\%$  and (from left to right)  $I_\phi = 0.0$  kA, 560 kA and 640 kA calculated by SPEC with the plasma boundary fixed.



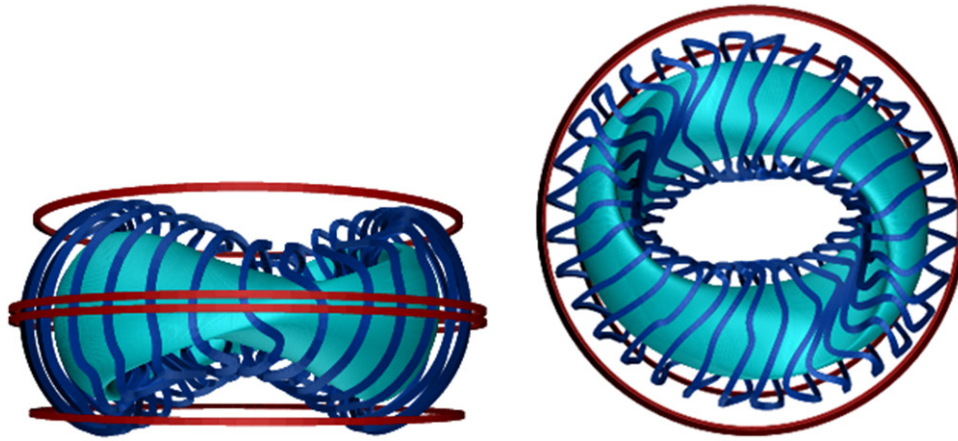
(a) Dependency of the mono-energetic radial transport coefficient  $D_{11}^*$  to collisionality. A banana regime is clearly visible at  $\nu^*$  between  $10^{-3}$  and  $10^{-2}$ .

(b) The mono-energetic bootstrap current  $D_{31}^*$  coefficient versus collisionality.

**Figure 14.** Mono-energetic transport coefficients [33] as calculated by DKES at  $r = 0.5$  with  $|B_{m,n}| > 0.0001$ : triangular shapes, for the new equilibrium design for  $E/vB$  between  $3 \times 10^{-3}$  and zero (black,  $3 \times 10^{-3}$ ; red,  $1 \times 10^{-3}$ ; blue,  $3 \times 10^{-4}$ ; orange,  $1 \times 10^{-4}$ ; green,  $3 \times 10^{-5}$ ; pink,  $1 \times 10^{-5}$ ; dark blue, zero); dotted line, transport coefficient for an equivalent tokamak case.

the two volumes separated by that surface, SPEC allows the plasma to explore *all possible* magnetic reconnection events that would lower the plasma potential energy. The equilibria thereby obtained with SPEC may not correctly describe the expected equilibria at given  $\beta$  and  $I_\phi$ , but rather represent the ‘worst-case scenario’ in which ‘maximal relaxation’ is allowed while supporting the prescribed pressure and current. We shall interpret the results as follows: whenever good flux surfaces are to be found despite the allowed relaxation, it shall be understood that no possible relaxation mechanism is likely to destroy these surfaces. When, on the other hand, islands and chaotic field lines are produced, it shall be inferred that this is the worst-case scenario and the potential destruction of flux surfaces is subject to the available relaxation and healing mechanisms.

Figure 11 shows examples of Poincaré sections of the equilibrium magnetic field obtained from SPEC calculations with increasing values of  $\beta$ , keeping  $I_\phi = 0$ . An island chain emerges at around  $\beta = 1.5\%$  and continuously increases in size. This is caused by the rotational transform crossing the resonance  $\iota = 2/6 = 1/3$  (see figure 12). A second scan is performed in which the total enclosed net toroidal current  $I_\phi$  is increased at fixed  $\beta = 3\%$ . Some illustrative Poincaré sections for different values of  $I_\phi$  are shown in figure 13. We remark that the effect of the net toroidal current on the rotational transform can be estimated as  $\iota \sim \mu_0 I_\phi R / (2\pi a^2 B_\phi)$ , where  $R$  is the major radius,  $a$  is the minor radius and  $B_\phi$  is the toroidal magnetic field. Since the location of the current in SPEC calculations is at about half the minor radius, the rotational transform relevant for this design is obtained for



(a) Side view of preliminary coils for the new equilibrium design with the original plasma boundary.

(b) Top view of preliminary coils for the new equilibrium design with the original plasma boundary.

**Figure 15.** Preliminary set of coils: a set of eight types of coil leads to 32 modular coils with an additional four poloidal field coils. The smallest radius of curvature appears near the quarter-period poloidal cross section, due to the strong plasma edge shaping.

$I_\phi \approx 600$  kA at reactor size. Around this value of current, we observe that the original region of  $\beta$ -induced islands and chaos are reduced (hence the current improves the quality of confinement), although other resonances around  $\iota = 2/5$  appear soon thereafter. We conclude that the designed equilibrium may not have chaotic regions but is clearly sensitive to the current within the plasma. Further investigations will be carried out in the future in order to gain confidence in these predictions. In particular, free-boundary SPEC calculations will be performed and the robustness of the magnetic topology will be assessed with respect to  $\beta$  and  $I_\phi$ .

### 3.5. Neoclassical transport and bootstrap current

The neoclassical mono-energetic transport coefficients [33] have been evaluated with DKES [34, 35]. Both the radial and bootstrap transport coefficients are close to the equivalent tokamak coefficients at half-radius (see figures 14(a) and (b)). Only at very small collisionality  $\nu^* < 10^{-3}$  do the coefficients depend on the electric field. A clear banana regime can be observed, which is relatively rare in stellarators [33] and provides further evidence for the minimization of the QA error near half-radius. At smaller and larger radii, the transport coefficients are more dependent on the electric field. This is in agreement with the effective ripple of this configuration (see figure 7(b)). It is worth emphasizing that the reduction of the effective ripple is a by-product; it was not optimized explicitly but is a result of reducing the QA error between  $s = 0.25$  and  $s = 0.5$ .

The bootstrap current has been evaluated with the NTSS code [21] for a hydrogen plasma in a configuration scaled to the same volume as ASDEX-Upgrade of around  $14.5 \text{ m}^3$  with a magnetic field of 2.5 T on-axis and with a volume-averaged  $\beta$  of 1.5%. The obtained bootstrap current was around 226 kA, which is close to the current used in the optimization (for this size it would be 250 kA for  $\beta \approx 3.5\%$ ). The rotational transform profile changes only slightly with the new

bootstrap current. We can therefore conclude that the configuration behaves similarly to a tokamak and that the anticipated bootstrap current is of the right order. Finally, the next and final section presents an initial description of the coil design.

### 3.6. Coils

Besides the physical properties depicted in this paper, engineering characteristics are also of great importance [36, 37]. A first investigation concerning the practicability of modular coils for a reactor-sized configuration have been performed with the ONSET code [38]. Four poloidal field coils have been employed with eight types of modular coil corresponding to a total of 32 modular coils (see figure 15). The coils have a maximum relative magnetic field error (given by  $e_l = |\mathbf{B} \cdot \mathbf{n}|/|\mathbf{B}|$  with  $\mathbf{B}$  the magnetic field on the plasma boundary and  $\mathbf{n}$  the normal vector of the plasma boundary) of around 4.1% and a mean relative magnetic field error ( $\int dA e_l/A$  with  $A$  the surface of the plasma boundary) of 0.95%. One can see that the most difficult shape for the coils is near the  $\phi = 45^\circ$  cross section (see figure 5(b)). Nevertheless, the clearance between the centreline of any two coils exceeds 51 cm everywhere for a reactor-size machine and the minimum radius of curvature is 63 cm. This is an encouraging first step in the coil design process, but further work has to be done.

## 4. Conclusion and future work

A new quasi-axisymmetric stellarator configuration has been designed to possess a number of favourable features. It was found by optimizing the curvature of the plasma boundary, the magnetic well, rotational transform and the quasi-axisymmetric field error. By varying the flux surface on which the quasi-axisymmetry was enforced, the optimization procedure was able to find configurations with particularly good neoclassical confinement.

The new plasma design has collisionless fast-particle loss rates below 8% for flux surfaces  $s \leq 0.25$ . We examined the ideal-MHD stability with CAS3D and found that it has a stability limit of  $\langle \beta \rangle \sim 3\%$ . The vacuum flux surfaces do not possess significant islands, but small ones appear when the current and beta are varied, but without the appearance of large stochastic regions. The neoclassical transport coefficients are nearly the same as in an equivalent tokamak at half-radius. The weakest point of our optimization is probably the coil design; however, this is still preliminary.

In future work, we aim to reduce the strong shaping at the plasma boundary seen at the  $\varphi = 45^\circ$  cross section (see figure 6(b)) to simplify the coil design. This might be possible by reducing the vacuum rotational transform while simultaneously checking MHD stability. Once improved coils have been found the confinement has to be verified.

Additionally, we will include a self-consistent bootstrap current into the optimization iteration to evaluate whether we can achieve all of these advantages. Further optimization work could seek to include ideal-MHD stability calculations and, if possible, check for stochastic fields inside the optimization loop. An appropriate divertor concept will also need to be found, which would feed back into the plasma boundary optimization.

Further, it has to be investigated whether the relatively large vacuum rotational transform is sufficiently large to avoid disruptions.

## Acknowledgments

The primary author would like to thank J. Nührenberg, J. Geiger and B. Shanahan for helpful conversations. This work has been carried out in the framework of the EUROfusion Consortium and has received funding from the Euratom research and training programme 2014–2018 under grant agreement no. 633053. The views and opinions expressed herein do not necessarily reflect those of the European Commission.

## ORCID iDs

S.A. Henneberg  <https://orcid.org/0000-0002-1949-7032>

C.D. Beidler  <https://orcid.org/0000-0002-4395-239X>

P. Helander  <https://orcid.org/0000-0002-0460-590X>

## References

- [1] Loizu J., Hudson S.R. and Nührenberg C. 2016 Verification of the SPEC code in stellarator geometries *Phys. Plasmas* **23** 112505
- [2] W VII-A Team 1980 Stabilization of the (2, 1) tearing mode and of the current disruption in the W VIIA stellarator *Nucl. Fusion* **20** 1093
- [3] Hirsch M. et al (The W7-AS Team) 2008 Major results from the stellarator Wendelstein 7-AS *Plasma Phys. Control. Fusion* **50** 053001
- [4] Pandya M.D. et al 2015 Low edge safety factor operation and passive disruption avoidance in current carrying plasmas by the addition of stellarator rotational transform *Phys. Plasmas* **22** 110702
- [5] Nührenberg J. and Zille R. 1988 Quasi-helically symmetric toroidal stellarators *Phys. Lett. A* **129** 113–7
- [6] Canik J.M., Anderson D.T., Anderson F.S.B., Likin K.M., Talmadge J.N. and Zhai K. 2007 Experimental demonstration of improved neoclassical transport with quasihelical symmetry *Phys. Rev. Lett.* **98** 085002
- [7] Canik J.M., Anderson D.T., Anderson F.S.B., Clark C., Likin K.M., Talmadge J.N. and Zhai K. 2007 Reduced particle and heat transport with quasisymmetry in the helically symmetric experiment *Phys. Plasmas* **14** 056107
- [8] Boozer A.H. 1995 Quasi-helical symmetry in stellarators *Plasma Phys. Control. Fusion* **37** A103
- [9] Boozer A.H. 1981 Plasma equilibrium with rational magnetic surfaces *Phys. Fluids* **24** 1999–2003
- [10] Helander P. 2014 Theory of plasma confinement in non-axisymmetric magnetic fields *Rep. Prog. Phys.* **77** 087001
- [11] Nührenberg J., Lotz W. and Gori S. 1994 Quasi-axisymmetric tokamaks *Theory of Fusion Plasmas, Varenna, 1994* (Bologna: Editrice Compositori) p 3
- [12] Garabedian P.R. 1996 Stellarators with the magnetic symmetry of a tokamak *Phys. Plasmas* **3** 2483–5
- [13] Nelson B.E. et al 2003 Design of the national compact stellarator experiment (NCSX) *Fusion Eng. Des.* **66** 169–74
- [14] Okamura S. et al 2001 Physics and engineering design of the low aspect ratio quasi-axisymmetric stellarator CHS-qa *Nucl. Fusion* **41** 1865
- [15] Drevlak M., Brochard F., Helander P., Kisslinger J., Mikhailov M., Nührenberg C., Nührenberg J. and Turkin Y. 2013 ESTELL: a quasi-toroidally symmetric stellarator *Contrib. Plasma Phys.* **53** 459–68
- [16] Drevlak M., Beidler C.B., Geiger J., Helander P. and Turkin Y. 2018 Optimisation of stellarator equilibria with ROSE *Nucl. Fusion* **59** 016010
- [17] Brent R.P. 1973 *Algorithms for Minimization without Derivatives* (Englewood Cliffs, NJ: Prentice Hall) ch 5
- [18] Hirshman S.P. and Whitson J.C. 1983 Steepest descent moment method for three dimensional magnetohydrodynamic equilibria *Phys. Fluids* **26** 3553–68
- [19] Merkel P. 1987 Solution of stellarator boundary value problems with external currents *Nucl. Fusion* **27** 867
- [20] Borchardt M. 2012 private communication
- [21] Turkin Yu., Maassberg H., Beidler C.D., Geiger J. and Marushchenko N.B. 2006 Current control by ECCD for W7-X *Fusion Sci. Technol.* **50** 387–94
- [22] Garren D.A. and Boozer A.H. 1991 Existence of quasihelically symmetric stellarators *Phys. Fluids B* **3** 2822–34
- [23] Plunk G.G. and Helander P. 2018 Quasi-axisymmetric magnetic fields: weakly non-axisymmetric case in a vacuum *J. Plasma Phys.* **84** 905840205
- [24] Shafranov V.D. and Zakharov L.E. 1972 Use of the virtual-casing principle in calculating the containing magnetic field in toroidal plasma systems *Nucl. Fusion* **12** 599
- [25] Nemov V.V., Kasilov S.V., Kernbichler W. and Heyn M.F. 1999 Evaluation of  $1/\nu$  neoclassical transport in stellarators *Phys. Plasmas* **6** 4622–32
- [26] Drevlak M., Geiger J., Helander P. and Turkin Y. 2014 Fast particle confinement with optimized coil currents in the W7-X stellarator *Nucl. Fusion* **54** 073002
- [27] Turkin Y., Beidler C.D., Maassberg H., Murakami S., Tribaldos V. and Wakasa A. 2011 Neoclassical transport simulations for stellarators *Phys. Plasmas* **18** 022505
- [28] Schwab C. 1993 Ideal magnetohydrodynamics: global mode analysis of three dimensional plasma configurations *Phys. Fluids B* **5** 3195–206

- [29] Rosenbluth M.N., Sagdeev R.Z., Taylor J.B. and Zaslavski G.M. 1966 Destruction of magnetic surfaces by magnetic field irregularities *Nucl. Fusion* **6** 297
- [30] Meiss J.D. 1992 Symplectic maps, variational principles, and transport *Rev. Mod. Phys.* **64** 795–848
- [31] Loizu J., Hudson S.R., Nührenberg C., Geiger J. and Helander P. 2017 Equilibrium  $\beta$ -limits in classical stellarators *J. Plasma Phys.* **83** 715830601
- [32] Hudson S.R., Dewar R.L., Dennis G., Hole M.J., McGann M., von Nessi G. and Lazerson S. 2012 Computation of multi-region relaxed magnetohydrodynamic equilibria *Phys. Plasmas* **19** 112502
- [33] Beidler C.D. et al 2011 Benchmarking of the mono-energetic transport coefficients—results from the International Collaboration on Neoclassical Transport in Stellarators (ICNTS) *Nucl. Fusion* **51** 076001
- [34] Hirshman S.P., Shaing K.C., van Rij W.I., Beasley C.O. Jr and Crume E.C. Jr 1986 Plasma transport coefficients for nonsymmetric toroidal confinement systems *Phys. Fluids* **29** 2951–9
- [35] van Rij W.I. and Hirshman S.P. 1989 Variational bounds for transport coefficients in three-dimensional toroidal plasmas *Phys. Fluids B* **1** 563–9
- [36] Brown T., Breslau J., Gates D., Pomphrey N. and Zolfghari A. 2015 Engineering optimization of stellarator coils lead to improvements in device maintenance *Presented at SOFE (Austin, TX, USA, 31 May–4 June 2015)* (<https://ieeexplore.ieee.org/document/7482426>)
- [37] Gates D.A. et al 2017 Recent advances in stellarator optimization *Nucl. Fusion* **57** 126064
- [38] Drevlak M. 1998 Automated optimization of stellarator coils *Fusion Technol.* **33** 106–17